








Article

Microplotter Printing of Co_3O_4 Films as Receptor Component of Hydrogen Sulfide-Sensitive Gas Sensors

Tatiana L. Simonenko ¹, Nikolay P. Simonenko ^{1,*}, Artem S. Mokrushin ¹, Philipp Yu. Gorobtsov ¹,
Ivan S. Vlasov ², Ivan A. Volkov ², Elizaveta P. Simonenko ¹ and Nikolay T. Kuznetsov ¹

¹ Kurnakov Institute of General and Inorganic Chemistry of the Russian Academy of Sciences, 31 Leninsky pr., 119991 Moscow, Russia

² Moscow Institute of Physics and Technology, National Research University, 9 Institutskiy per., 141701 Dolgoprudny, Russia

* Correspondence: n_simonenko@mail.ru

Abstract: A hierarchically organized Co_3O_4 nanopowder was obtained via programmed chemical precipitation, exhibiting several levels of microstructural self-organization: the initial particles are 40 ± 5 nm in size (average CSR size is 32 ± 3 nm), have a somewhat distorted rounded shape and are combined into curved chains, which, in turn, form flat agglomerates of approximately 350 ± 50 nm in diameter. The thermal behavior of the semiproduct ($\beta\text{-Co}(\text{OH})_2$) was studied by means of a synchronous thermal analysis (TGA/DSC). The obtained powders were examined by X-ray diffraction analysis (XRD) and Fourier-transform infrared spectroscopy (FTIR). Nanopowder of cobalt(II,III) oxide was employed as a functional ink component for the microplotter printing of the corresponding film on the chip surface, and the preservation of the material's crystal structure was confirmed by XRD and Raman spectroscopy (RS). The microstructural features of the resulting film were analyzed by scanning electron microscopy (SEM) and atomic force microscopy (AFM). Kelvin probe force microscopy (KPFM) was utilized to estimate the work function of the material surface, and the scanning capacitance microscopy (SCM) data indicated the intergranular conductivity type. The results of the conducted chemosensor measurements demonstrate that the printed Co_3O_4 film exhibits hydrogen sulfide selectivity and a rather high sensory response ($S = 131\%$ for 100 ppm) to this analyte at an operating temperature of 250°C . The dependence of the sensor response value and time when detecting H_2S in the concentration range of 4–200 ppm was determined and the high reproducibility of the signal was demonstrated.

Keywords: Co_3O_4 ; programmable coprecipitation; hierarchical structure; gas sensor; hydrogen sulfide



Citation: Simonenko, T.L.; Simonenko, N.P.; Mokrushin, A.S.; Gorobtsov, P.Y.; Vlasov, I.S.; Volkov, I.A.; Simonenko, E.P.; Kuznetsov, N.T. Microplotter Printing of Co_3O_4 Films as Receptor Component of Hydrogen Sulfide-Sensitive Gas Sensors. *Chemosensors* **2023**, *11*, 166. <https://doi.org/10.3390/chemosensors11030166>

Academic Editors: Estefanía Núñez Carmona and Veronica Sberveglieri

Received: 31 January 2023
Revised: 22 February 2023
Accepted: 27 February 2023
Published: 1 March 2023



Copyright: © 2023 by the authors. Licensee MDPI, Basel, Switzerland. This article is an open access article distributed under the terms and conditions of the Creative Commons Attribution (CC BY) license (<https://creativecommons.org/licenses/by/4.0/>).

1. Introduction

Hydrogen sulfide is a colorless, flammable toxic gas whose formation as a byproduct is associated with technological processes in a number of industrial branches; in particular, oil, gas, mining, pulp, the pharmaceutical sector, etc. [1,2]. The limits of acceptable H_2S concentrations according to international standards range from 10 to 50 ppm [3]. Exposure to low concentrations of H_2S has a negative effect on the human nervous, digestive and respiratory systems, while high concentrations can be lethal. In humid atmospheres, this gas can become a source of construction material corrosion [4]. In this regard, the development of methods for creating effective receptor components of gas sensors with a high sensitivity and selectivity in relation to hydrogen sulfide remains extremely urgent today. There are a fairly large number of high-performance approaches to analyzing the ambient atmosphere (e.g., laser absorption [5], tunable diode laser absorption spectroscopy (TDLAS) [6] and light-induced thermoelastic spectroscopy (LITES) [7]); however, resistive gas sensors are known to have significant advantages, such as a low cost and portability [8], which ensures their wide adoption in various applications.

Especially promising in this context are semiconducting metal oxides [9,10]; in particular, Co_3O_4 , characterized by a high redox activity and electrical conductivity, commercial availability and also, depending on the method of production, demonstrating selectivity to gases such as ammonia [11], hydrogen [12] and carbon monoxide [13] and a range of volatile organic compounds (n-butanol [14], acetone [15], toluene and xylene [16]).

It is known that the surface microstructure of the receptor material has a significant influence on the gas detection kinetics, as well as on the sensor response values. The formation of hierarchically organized nanomaterials characterized by a high specific surface area that, in turn, increases the number of its active centers and the charge transfer rate, allowing us to improve the electrophysical properties of the resulting materials, has attracted an increasing interest from the scientific community in recent years [17,18]. The number of works devoted to proving the efficiency of 0–3D hierarchical nanomaterials as resistive gas sensor components for various analyte gases is growing rapidly [19–23].

The most popular methods for anisotropic material formation are hydrothermal synthesis [24–27], sol–gel technology [28,29], electrospinning [30,31], electrodeposition [32–35] and the combined chemical precipitation of hydroxides [36,37], carbonates [38,39] or metal oxalates [40,41]. Thus, in the case of hydrothermal synthesis, anisotropic nanostructures of different types can be obtained, which differ in their selectivity for detecting a particular analyte [26]. Sol–gel technology is usually characterized by the formation of highly dispersed primary particles organized into three-dimensional spatial agglomerates with a high porosity and, consequently, sorption capacity [29]. One-dimensional nanomaterials are formed using electrospinning, where the microstructural character significantly affects the electrochemical characteristics [30]. Using electrochemical deposition [34], as in the case of hydrothermal synthesis, hierarchically organized cellular structures (including core–shell-type) with a complex structure of pores and channels can be formed on substrates of a complex shape, which ensures the high activity of the material surface. Chemical precipitation is one of the easiest and most convenient methods in terms of the equipment used, allowing, depending on the synthesis conditions, for the formation of both isotropic and hierarchically organized nanomaterials (including ones with a complex composition), which differ in their functional properties [36]. In this work, we propose the usage of programmed chemical precipitation, which enables a high degree of automation of the synthesis process and fine control of its parameters (continuous or discrete precipitant feeding to the metal-containing reagent solution in a wide range of rates and volumes with the consideration of temperature and pH values in the reaction system measured simultaneously). In turn, this makes it possible to significantly increase the reproducibility of the microstructural and functional features of the formed material [42].

The target operational characteristics of the resulting planar nanostructures can be preset not only at the synthesis stage but also at the stage of applying the appropriate coating to the substrate. Given the recent trends toward smaller components and devices in microelectronics and gas sensing, specialists in this field are increasingly striving to combine synthetic approaches with additive technologies that solve the issues of planarization and miniaturization by the targeted deposition of the active material of the desired composition, constituting a corresponding functional ink, on the desired area of the substrate [43,44]. The most common and demanded methods in this context are ink-jet printing [45–48], aerosol printing [49–54], microplotting [42,55–57] and microextrusion [58–63], as well as pen plotter printing [42,64,65]), which enable the reproducible coatings of the desired thickness and geometry on various substrates in automatic mode according to the specified digital model.

The aim of the present work was to study the synthesis of hierarchically organized cobalt(II,III) oxide using programmed chemical precipitation and develop a technique for the microplotter printing of the corresponding film, as well as to examine the chemosensory properties of the resulting material; in particular, when detecting hydrogen sulfide.

2. Materials and Methods

2.1. Materials

$\text{Co}(\text{NO}_3)_2 \cdot 6\text{H}_2\text{O}$ (99%, Chimmed, Moscow, Russia) and 5% aqueous solution of $\text{NH}_3 \cdot \text{H}_2\text{O}$ (Chimmed, Moscow, Russia), α -terpineol (>97%, Vekton, Russia) and ethyl cellulose (48.0–49.5% (*w/w*) ethoxyl basis, Sigma Aldrich, Saint Louis, MO, USA) were used in this work without further purification.

2.2. Oxide Nanopowder Preparation

Preparation of Co_3O_4 nanopowder was carried out by programmed chemical precipitation using an ATP-02 potentiometric titrator (Aquilon JSC, Podolsk, Russia). Thus, automatic addition (supply pulse was 2 s with a pause between each pulse of 1 s) of ammonia hydrate solution to an aqueous solution of cobalt nitrate ($c = 0.1 \text{ mol/L}$) under stirring was carried out until reaching $\text{pH} = 9.2$ and complete precipitation of the semiproduct particles. The resulting precipitate was separated from the mother liquor and washed with distilled water by cyclic centrifugation, and then dried at $100 \text{ }^\circ\text{C}$ until mass stabilization (within 3 h). Further, based on the results of synchronous thermal analysis of the powder obtained, the regime of its additional heat treatment ($500 \text{ }^\circ\text{C}$, 1 h) for the purpose of complete decomposition and crystallization of Co_3O_4 was determined.

2.3. Microplotter Printing of Co_3O_4 Film

The resulting hierarchically organized Co_3O_4 nanopowder was further used to prepare a stable disperse system (solid phase particle content was 8 wt%) in α -terpineol in the presence of a binder (ethylcellulose), suitable as a functional ink for microplotter printing (Microplotter II, Sonoplot Inc., Middleton, WI, USA) of cobalt(II,III) oxide film on the specialized Pt/ Al_2O_3 /Pt chip ($R_a = 100 \text{ nm}$, geometric dimensions $4.1 \times 25.5 \times 0.6 \text{ mm}$). A capillary with a nozzle diameter of $60 \text{ }\mu\text{m}$ was used as a dispenser. An ink layer of $5 \times 3 \text{ mm}$ in the lateral plane was applied to the chip surface in the area of preapplied platinum interdigitated electrodes automatically according to a prearranged digital trajectory. The applied ink film was then subjected to step drying in the temperature range of $25\text{--}60 \text{ }^\circ\text{C}$ (4 h) until complete evaporation of the solvent, followed by an additional heat treatment at $400 \text{ }^\circ\text{C}$ for 1 h to remove the binder.

2.4. Instrumentation

The thermal behavior of the obtained semiproduct was studied by synchronous (TGA/DSC) thermal analysis (SDT Q-600 thermal analyzer, TA Instruments, New Castle, DE, USA) in an air flow in the temperature range $25\text{--}1000 \text{ }^\circ\text{C}$ (controlled heating was performed in Al_2O_3 -microcrucibles at a rate of $10^\circ/\text{min}$ in an air flow, gas flow rate was 250 mL/min and sample mass was 14.966 mg).

To register the Fourier-transform infrared spectra of the powders, the corresponding suspensions were prepared in Vaseline oil, and were then placed between KBr glasses as films. Spectra were recorded in the wavenumber range of $350\text{--}4000 \text{ cm}^{-1}$ (signal accumulation time— 15 s , resolution— 1 cm^{-1}) using an Infra-LUM FT-08 FTIR-spectrometer (Lumex, St. Petersburg, Russia).

X-ray diffraction analysis of the obtained powders was carried out with a D8 Advance diffractometer (Bruker, Bremen, Germany; $\text{CuK}\alpha = 1.5418 \text{ \AA}$, Ni-filter, $E = 40 \text{ keV}$, $I = 40 \text{ mA}$, 2θ range— $10^\circ\text{--}80^\circ$, resolution— 0.02° , signal accumulation time in the point was 0.3 s).

The Raman spectrum of the oxide film was recorded with an R532 spectrometer (EnSpectr, Chernogolovka, Russia) in the wavenumber range of $150\text{--}4000 \text{ cm}^{-1}$ (scan accumulation time— 200 ms , number of scans— 200 , laser wavelength— 532 nm).

The microstructures of the obtained Co_3O_4 nanopowder and the corresponding oxide film were analyzed by scanning electron microscopy (NVision-40, Carl Zeiss, Inc., Oberkochen, Germany). Elemental analysis of the materials was performed within the framework of SEM using an EDX spectrometer INCA X-MAX 80 (Oxford Instruments, Abingdon, UK).

The prepared Co_3O_4 film was also examined by atomic force microscopy. As a result of the measurements, we obtained data on the material microstructure and its local electro-physical properties. For this purpose, Solver Pro-M scanning probe microscope (NT-MDT, Zelenograd, Russia) and ETALON HA-HR probes (ScanSens, Bremen, Germany) with a conductive coating based on tungsten carbide (resonance frequency ~ 213 kHz) were used. Scanning was performed in modes of semicontact AFM, Kelvin probe scanning microscopy and scanning capacitive microscopy. The measurements were performed in air.

The chemosensor features were tested in a specialized setup. The gas environment was created inside a quartz chamber using two Bronkhorst (Nijverheidsstraat, The Netherlands) gas flow controllers with a maximum flow rate of 100 and 200 mL/min. The temperature of the sensor element was controlled using a platinum microheater embedded in the chip. The resulting film was studied for detection of H_2 , CO, NH_3 , NO_2 and H_2S . The material resistance was measured using a Fluke 8846A digital multimeter (6.5 Digit Precision Multimeter, Everett, WA, USA) with an upper limit of 1 G Ω . Synthetic air was used as the baseline gas. The sensory response values were calculated using the following formula:

$$S = |R_g - R_{\text{Air}}| / R_{\text{Air}}, \quad (1)$$

where R_g is a resistance at a given analyte gas concentration and R_{Air} is the resistance in air.

3. Results and Discussion

3.1. Characterization of the Intermediate Product and the Obtained Oxide Nanopowder

A thermal analysis (TGA/DSC) was carried out to investigate the semi-product behavior in an air flow in the temperature range of 25–1000 °C (Figure 1). Thermograms indicate that the powder heating leads to a five-step weight loss in the temperature intervals of 25–140, 140–190, 190–275, 275–900 and 900–930 °C. In the first step, residual solvent and sorbed atmospheric gases are removed from the powder surface, and the corresponding Δm value is approximately 1%. At the next stage, there is a sharp decrease in mass ($\sim 7\%$) accompanied by an exothermic effect with a maximum at 167 °C, which is probably associated with Co^{2+} to Co^{3+} oxidation and Co_3O_4 formation [66], accompanied by the intermediate product (presumably, $\text{Co}(\text{OH})_2$) decomposition. The third step of mass loss ($\Delta m = 5\%$) is associated with the endo effect at a minimum of around 259 °C and refers to cobalt hydroxide degradation. This process continues in the next stage with a 2.4% mass loss, but slows down significantly after reaching 400 °C. A sharp decrease in mass ($\sim 5.6\%$) and a corresponding endothermic effect with an extremum at 924 °C take place in the temperature region of 900–930 °C, which refers to the transformation of Co_3O_4 to CoO with oxygen emission. Thus, the total mass loss for the intermediate product in the investigated temperature range is approximately 21%. Taking into account the thermal analysis data, the optimal mode of the additional heat treatment of powder (500 °C, 1 h) providing a complete semi-product decomposition and preservation of its highly dispersed state is determined.

The set of functional groups in the semi-product and the obtained oxide powder was studied using FTIR (Figure 2). Thus, a narrow absorption band with a maximum at 3632 cm^{-1} related to the hydroxyl groups ($-\text{OH}$) stretching vibration mode of the non-hydrogen bond [67], which is typical for $\beta\text{-Co}(\text{OH})_2$, was observed in the spectrum of the semi-product after its drying at 100 °C for 3 h. The also-present absorption band with a maximum at 490 cm^{-1} refers to $\nu(\text{Co}-\text{O})$ stretching vibrations [67,68]. The results of the spectral analysis of the oxide powder reveal two absorption bands with maximums at 561 and 661 cm^{-1} , which are characteristic for cobalt(II,III) oxide and refer to the stretching vibrations of the $\text{Co}-\text{O}$ ($\text{Co}^{3+}-\text{O}$) bond and the bridging vibration of the $\text{Co}-\text{O}$ ($\text{Co}^{2+}-\text{O}$) bond, respectively. These peaks result from the octahedral and tetrahedral sites of the spinel structure of the Co_3O_4 nanoparticles [69,70]. Thus, the FTIR results indicate the formation of cobalt(II) hydroxide in β -modification as the intermediate product, while heat

treatment at 500 °C leads to its complete decomposition and cobalt(II,III) oxide formation. No impurities related to reagents or by-products were found in the powders.

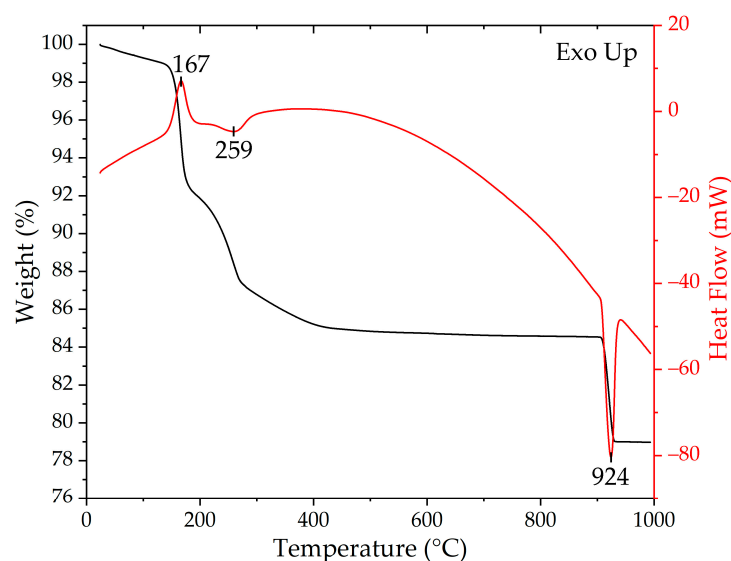


Figure 1. Results of synchronous (TGA/DSC) thermal analysis of the semi-product obtained.

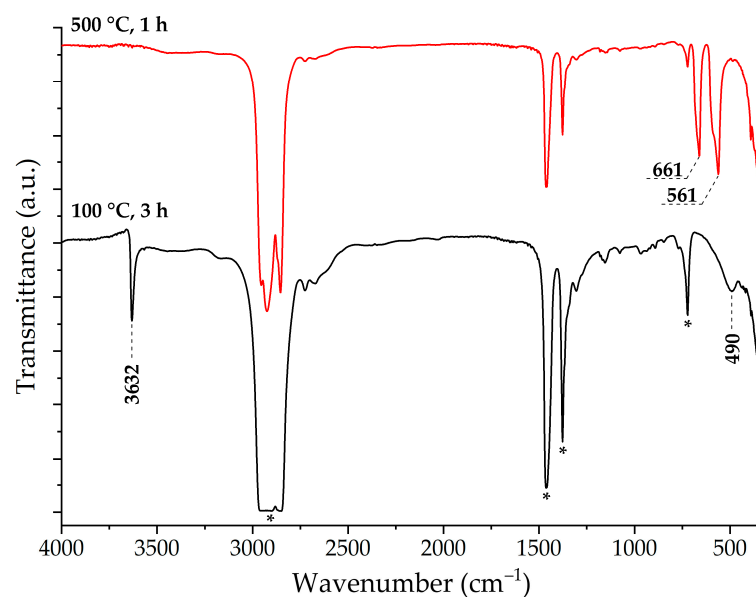


Figure 2. FTIR spectra of the obtained semi-product (**bottom**) and oxide powder (**top**); the marker “*” refers to the absorption bands of Vaseline oil.

The crystal structure of the semi-product and the oxide powder obtained by its additional heat treatment was investigated by X-ray diffraction analysis (Figure 3). As can be seen from the corresponding X-ray diffraction pattern, the reflection set for the intermediate belongs to the β -Co(OH)₂ hexagonal phase (JCPDS card #74-1057) [71], and there are no signals from any crystalline impurities. The average size of the coherent scattering regions (CSRs) for this powder was 28 ± 3 nm. The analysis of the crystal structure of the obtained oxide powder testifies to the formation of face-centered cubic phase of cobalt(II,III) oxide (JCPDS card #42-1467) [72]. At the same time, no reflections from any by-products and the semi-product used were detected on the material diffractogram, suggesting its complete conversion and, accordingly, the choice of the optimal mode of additional heat treatment. The average CSR size for the obtained Co₃O₄ powder was 32 ± 3 nm, which indicates an insignificant (~14%) increase in the material crystallites compared to the semi-product

(primarily due to the additional high-temperature treatment). Thus, it was shown that the proposed approach to the cobalt(II,III) oxide synthesis using the programmed chemical deposition method allows for the formation of single-phase nanocrystalline powder with the target crystalline structure.

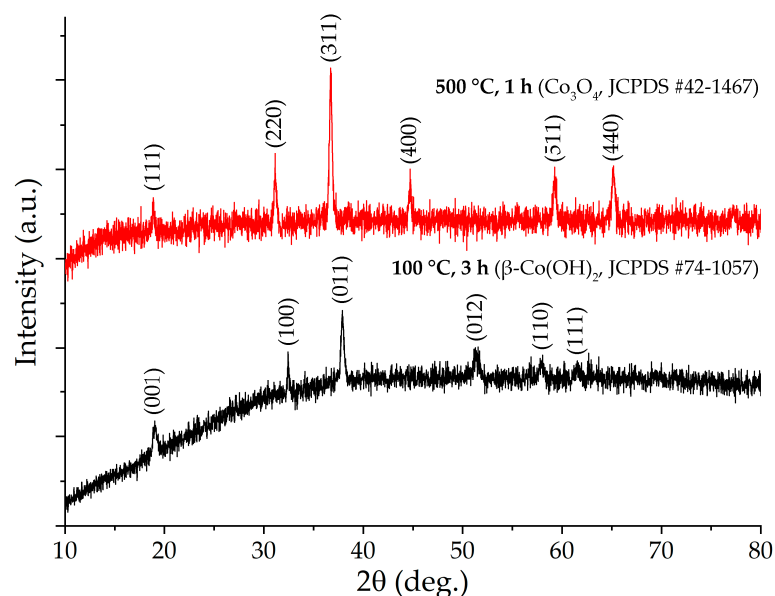


Figure 3. X-ray diffraction patterns of the semi-product (**bottom**) and the oxide powder obtained (**top**).

The microstructural features of the prepared Co_3O_4 powder were analyzed by scanning electron microscopy (Figure 4). The micrographs show that the powder has several levels of organization. Thus, the initial particles have a slightly deformed circular shape and their average size is 40 ± 5 nm (Figure 4c,d), which agrees reasonably well with the size of the CSR determined by X-ray diffraction analysis. These particles are further arranged into curved chains that combine to form flat agglomerates of approximately 350 ± 50 nm in diameter (Figure 4a,b). The morphology of the powder is homogeneous and no formations with different dispersity and geometrical parameters are observed. Presumably, this microstructure of the powder is due to the nature of the semi-product ($\beta\text{-Co(OH)}_2$) formed at the first synthetic stage, for which, due to the type of crystal lattice, a tendency to form hexagonal plates is often observed [73]. Their further heat treatment can lead to the microstructure transformation and development of more porous structures. Thus, the investigation of the resulting oxide powder microstructure testifies to its nanoscale state and hierarchical self-organization of primary 0D nanoparticles into 1D chains, which, in turn, are combined into 2D agglomerates. The results of the energy dispersive X-ray microanalysis performed in the framework of SEM indicate the absence of any impurities differing in the chemical composition from the basic material.

3.2. Characterization of the Printed Co_3O_4 Film

The surface of the formed oxide film was examined by Raman spectroscopy (Figure 5). According to the spectrum obtained, a set of bands with maxima at 474, 520, 608 and 686 cm^{-1} , corresponding to the E_g , $2 \times F_{2g}$ and A_{1g} vibrational modes of Co_3O_4 , are observed for the material under study [74]. The A_{1g} vibrational mode is the typical characteristic of Co^{3+} located at the cationic sublattice (octahedral positions), whereas the E_g and F_{2g} modes are likely related to the combined vibrations of tetrahedral site and octahedral oxygen motions [75]. The full width at half maxima (FWHM) of the peak corresponding to the A_{1g} mode in our case has a value of 26, indicating the nanoscale state of the material. Thus, the results of Raman spectroscopy confirm the preservation of the crystal lattice type of cobalt(II,III) oxide after functional ink preparation with the corresponding nanopowder and the formation of Co_3O_4 film with its subsequent additional heat treatment. The spectrum

of the studied material also shows signals from the Al_2O_3 substrate, suggesting a small thickness of the oxide film.

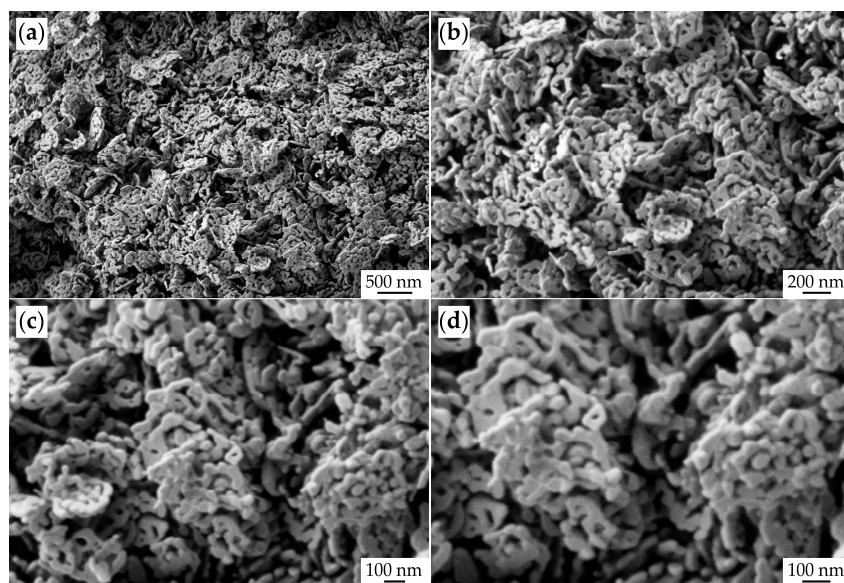


Figure 4. Microstructure of the obtained Co_3O_4 nanopowder (according to SEM data; $\times 50$ k (a), $\times 100$ k (b), $\times 150$ k (c), $\times 200$ k (d)).

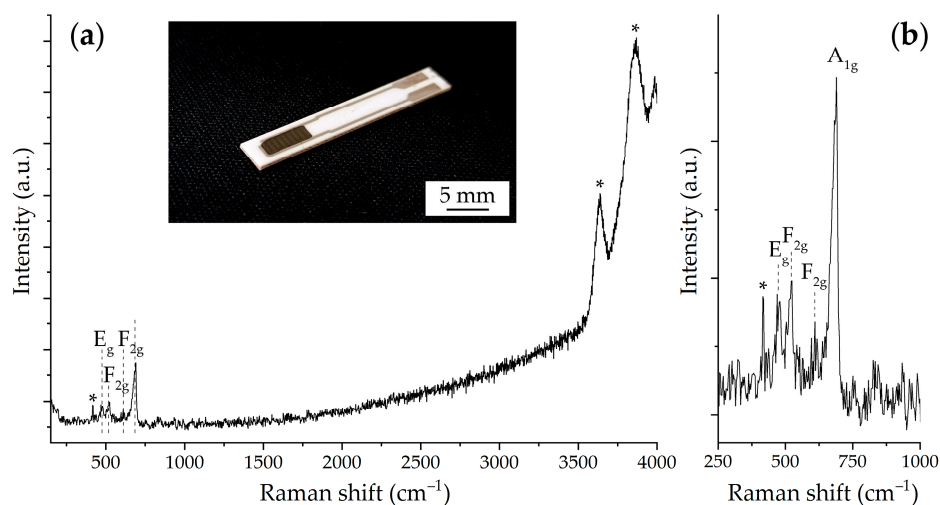


Figure 5. Raman spectra of the developed Co_3O_4 film: ((a) overview spectrum, (b) spectrum in the $250\text{--}1000\text{ cm}^{-1}$ range; marker “*” indicates Al_2O_3 substrate signals), as well as the appearance of the chip with the printed oxide film.

The crystal structure of the oxide film deposited on the Pt/ Al_2O_3 /Pt chip was also studied by X-ray diffraction analysis (Figure 6). It can be seen that the reflection set of the studied film corresponds to the face-centered cubic phase of cobalt(II,III) oxide (JCPDS card #42-1467), as in the case of the nanopowder employed. During the microplotter printing and additional heat treatment of the film, no crystalline impurities appeared, and the average CSR size for the resulting planar structure was 29 ± 3 nm. Therefore, during the Co_3O_4 film formation, there was some decrease in this parameter compared to the oxide powder used, which may be related to the partial dissolution of solid-phase particles in α -terpineol in the course of functional ink preparation. Since the intensity of the reflexes related to the cobalt(II,III) oxide film is significantly lower compared to the signals from the aluminum oxide and platinum oxide composing the chip, the film is rather thin.

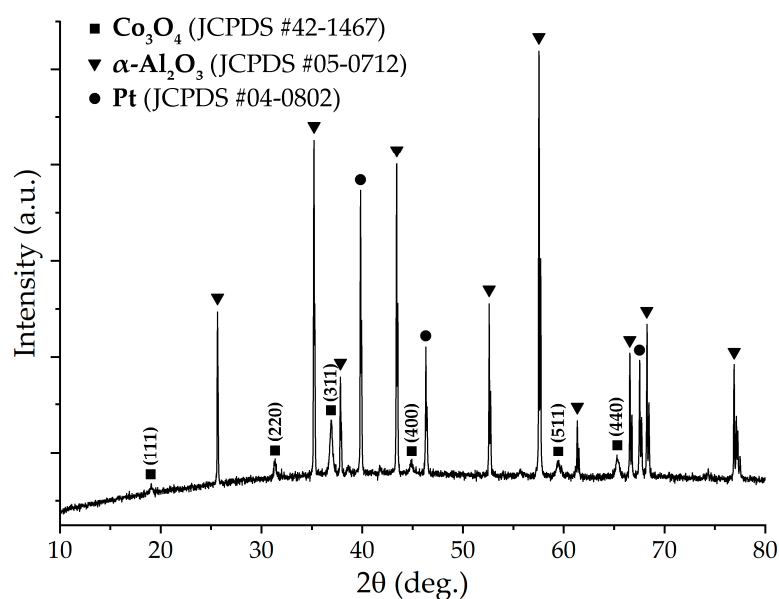


Figure 6. XRD pattern of Co_3O_4 film printed on the Pt/ Al_2O_3 /Pt chip surface.

The morphology of the printed cobalt(II,III) oxide film was analyzed by scanning electron microscopy (Figure 7). As seen from the data obtained, the character of the microstructure is generally similar to that of the oxide nanopowder used. Thus, the film is composed of two-dimensional agglomerates consisting of chains of nanoparticles with a rounded or slightly elongated shape (Figure 7a,b). As a difference from the previously mentioned powder, we should note a smaller size of primary nanoparticles (35 ± 5 nm), which may be due to their partial dissolution in α -terpineol at the stage of functional ink preparation, agreeing well with the XRD results. Consequently, the dispersity of the obtained Co_3O_4 film was further increased due to this effect. In general, the oxide film is characterized by a sufficiently high porosity, which is an important parameter for the resistive gas sensor receptor components, and the pore size is in a wide range, varying from 10 to 500 nm (Figure 7c,d). Thus, the findings confirm the preservation of the microstructural features of the hierarchically organized nanosized cobalt(II,III) oxide synthesized by programmed chemical deposition after the microplotter printing of the corresponding film on the chip surface.

The surface of the printed Co_3O_4 film was also studied by atomic force microscopy (Figure 8). It is clear from the topographic images (Figure 8a,b) that the film is nanoscale and continuous. The film consists of slightly elongated round particles 70–140 nm long. Toward the apex, their width decreases and reaches two to three tens of nanometers. This picture is somewhat different from the SEM results, which can be explained by the effect of the shape of the tip of the probe used. The mean square roughness of the surface was 46 nm. The thickness of the formed oxide film was also determined by atomic force microscopy, which was approximately 5 μm .

In addition to the surface topography of the film, its local electrophysical properties, such as the distribution of the surface potential and the capacitance gradient over the surface, were studied. Thus, the surface potential (Figure 8c) is distributed over the surface very uniformly: fluctuations in this parameter in the studied area are just ± 10 mV, which indicates a relatively high conductivity of the material, due to which, there is no large accumulation of charge on individual sections of the film. From the map of the capacitance gradient distribution for the “probe tip–sample microregion” capacitor (Figure 8d) we can see that an increased gradient (lighter areas) is observed in the areas at the boundaries between the oxide particles. Such behavior may indicate a pronounced intergranular character of the film conductivity.

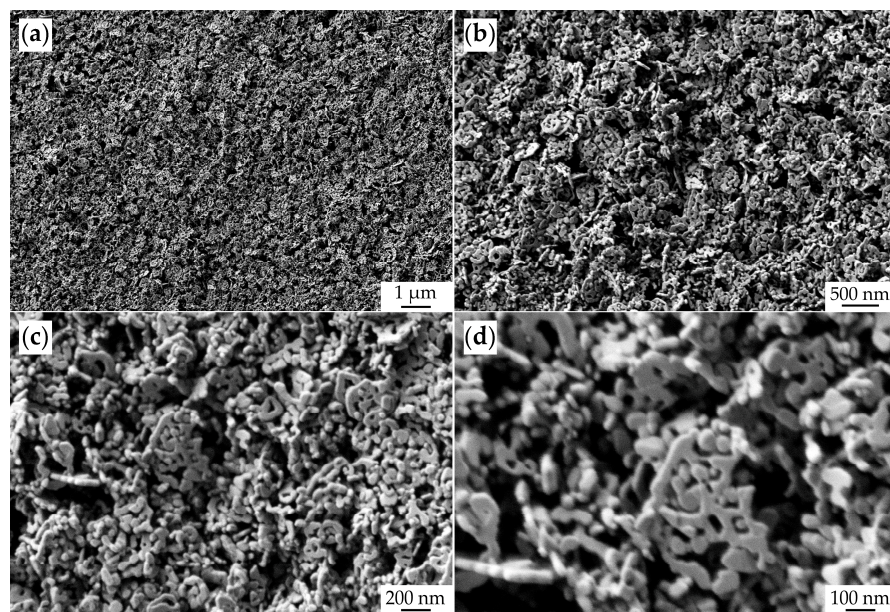


Figure 7. Microstructure of the printed Co_3O_4 film (according to SEM data; $\times 20\text{ k}$ (a), $\times 50\text{ k}$ (b), $\times 100\text{ k}$ (c), $\times 200\text{ k}$ (d)).

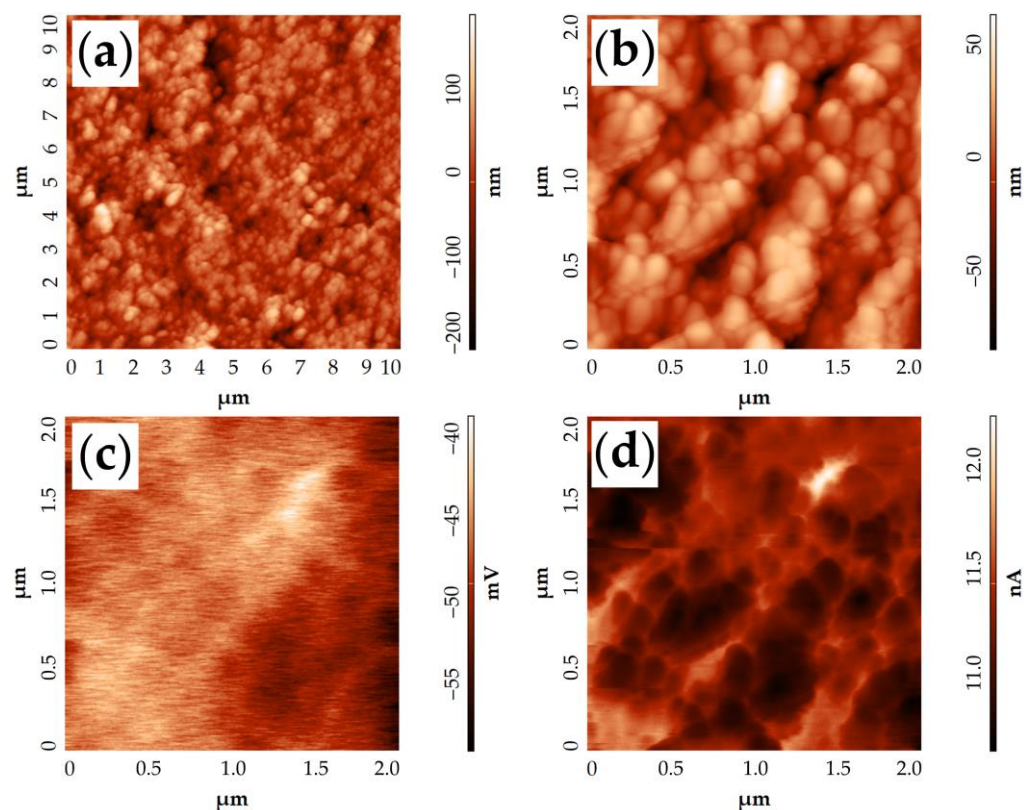


Figure 8. Co_3O_4 film AFM results: topography (a,b), surface potential distribution map (c) and capacitance gradient distribution map of “probe tip–sample microregion” capacitor (d).

In addition to mapping the surface potential distribution over the surface of the oxide film, the electron work function value for the film surface was also calculated using the results of the KPFM. The value of this parameter was 4.62 eV, which is lower than the values usually found in the literature (5.1–6.2 eV) for Co_3O_4 [76–78]. At the same time, this range is based on measurements and calculations in a vacuum. Our measurements

were performed in the presence of air, which leads to the sorption of atmospheric gases and water molecules on the material surface, due to which, the value of the electron work function can significantly decrease.

3.3. Chemosensory Properties of Co_3O_4 Film

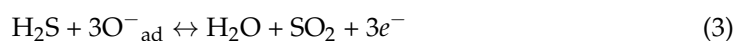
In the first step, the chemoresistive responses for the printed Co_3O_4 film were sequentially determined for the following gases at given concentrations: 100 ppm CO, 100 ppm NH_3 , 2000 ppm H_2 , 100 ppm NO_2 and 100 ppm H_2S . Sensor responses were measured at operating temperatures of 50–400 °C in intervals of 50 °C. As a result, an oxide film selectivity diagram was plotted, demonstrating the dependence of its sensory response on the above analytes over the temperature range considered (Figure 9a). At 400 °C, the response of the oxide film to all analyzed gases is zero. When proceeding to lower operating temperatures, there is a noticeable sensitivity to the analytes under investigation. The S value of 100 ppm NH_3 and CO is 1–97% and 1.5–195%, respectively, and, in the case of 2000 ppm H_2 , it is in the range of 6–72%. The maximum signal values are observed at 150 °C. A significant sensitivity of the material to NO_2 was found at lower temperatures, and the maximum sensor response value (158%) was observed at 100 °C. At 50 °C, a noticeable response ($S = 71\%$) was found only for nitrogen dioxide. While at high operating temperatures (350–250 °C), the responses to NH_3 , H_2 , CO and NO_2 were not that high (no more than 42%), the response to H_2S was found to be the highest (16–182%, with a maximum at 150 °C) over the entire temperature range (100–350 °C). In order to select the optimal operating temperature of detection, several sensing characteristics should be considered: first of all, the selectivity, as well as the sensor response value. According to the selectivity diagram (Figure 9a), the optimal operating temperature for the Co_3O_4 film under study is 250 °C when the high response to hydrogen sulfide ($S = 131\%$) and the low sensitivity to other analyte gases (S does not exceed 42%) are combined. At this temperature, the chemosensor properties of the material upon H_2S detection were studied in more detail.

The detection mechanism for the Co_3O_4 receptor material is classical for p-type semiconductors within chemoresistive gas sensors. In an air environment at elevated temperatures, oxygen molecules adsorb on the semiconductor surface, which leads to a change in the resistance of the material. Electrons from the conduction zone reduce O_2 to the ionic form:



Depending on the operating temperature, the formation of O^{2-} , O^- and O_{2-} ion-adsorbed forms is possible [79]. At the intermediate operating temperatures (150–400 °C), O -particles are characteristic. The presence of such ions on the p-type semiconductor surface promotes the formation of a core–shell electronic structure, where the core is the particles on the semiconductor surface, and the shell is the hole accumulation layer (HAL) formed as a result of electron consumption for O_2 reduction. In the analyte gas environment, a redox reaction (ORR) occurs at the semiconductor surface between oxygen-ion-adsorbed forms (O^{2-} , O^- and O_{2-}) and a gas, where the latter is oxidized (in the case of the redox gas—in our work, it is CO, NH_3 , H_2 and H_2S) or reduced (for the oxidant gas—in our case, it is NO_2). Thereby, the electrons that are released as a result of the ORR recombine with holes, which leads to a change in resistance and enables us to register a resistive response.

The equation for the possible resistive response when detecting H_2S with cobalt(II,III) oxide can be expressed as follows [80,81]:



Reaction (3) is an equilibrium, so the resistance should gradually return to the initial baseline values after the analyte gas is cut off.

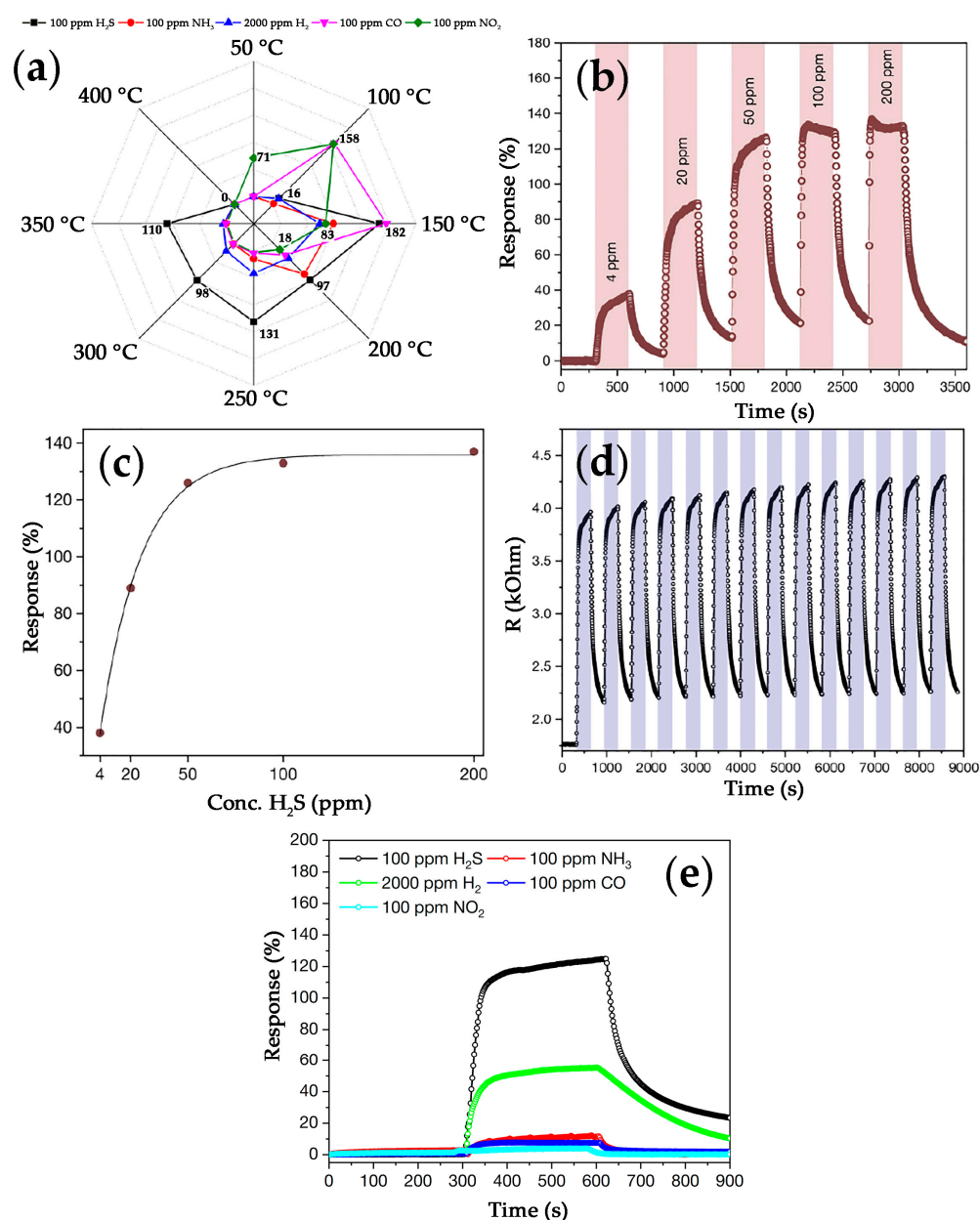


Figure 9. Selectivity diagram showing responses to 100 ppm H₂S, NH₃, CO, NO₂ и 2000 ppm H₂ at different operating temperatures with numerical values of sensor response to H₂S and NO₂ (a), signal reproducibility upon detecting 50 ppm H₂S at 250 °C (b), experimental data upon detecting 4–200 ppm H₂S at 250 °C (c), dependence of sensor response value on H₂S concentration at 250 °C (d) and the sensor response shape when detecting the analytes under study at 250 °C (e).

The chemosensor properties of the printed oxide film when detecting H₂S in the concentration range of 4–200 ppm were studied (Figure 9b). It can be seen that, as the hydrogen sulfide concentration increases from 4 ppm to 200 ppm, the sensory response at 250 °C improves from 38% to 137%. While, at relatively low concentrations (4–50 ppm) of this gas, a linear dependence of a given signal is observed, a saturation and stabilization of the sensor response value takes place as the analyte concentration increases (Figure 9c). This relation is power-dependent and is well described by the Freundlich adsorption isotherm equation [82]. Such a character of the dependence is typical for chemoresistive gas sensors [81]. The calculated response times (t_{90}) also correlate well with the above relationship: the response time decreases from 190 to 9 s when the H₂S concentration increases from 4 to 200 ppm. The reproducibility of the chemoresistive response was

studied when detecting 20 ppm hydrogen sulfide (Figure 9d). Thus, a small signal drift was observed during the first gas injections, followed by the signal stabilization. This phenomenon is related to the reaction (3), when the forward and reverse reaction rates differ, although an equilibrium is reached with time. The sensor response shapes for various analytes were examined in this work (Figure 9e). As can be seen from the plot, the signals have a shape that is close to rectangular, which is optimal for chemoresistive gas sensors.

When comparing the data obtained with our previous results for a Co_3O_4 thin film formed by the combination of sol-gel technology and pen plotter printing [83], it should be noted that the increased film thickness and the hierarchical organization of the receptor material contribute to an increase in the response value for the analytes examined. In the current study, the high efficiency of hydrogen sulfide detection is achieved due to the microstructural features of the material, with no need to modify cobalt(II,III) oxide with oxides of other metals [84,85] or carbon structures [86].

4. Conclusions

Hierarchically organized Co_3O_4 nanopowder was synthesized by programmed chemical precipitation. It was found that the $\beta\text{-Co(OH)}_2$ hexagonal phase with an average CSR size of 28 ± 3 nm was formed as an intermediate product, which, according to thermal analysis, is completely transformed into cobalt(II,III) oxide during an additional heat treatment in the air at 500°C for 1 h. SEM data revealed that the oxide powder has several levels of microstructural self-organization: primary particles 40 ± 5 nm in size (average CSR size was 32 ± 3 nm) have a slightly distorted circular shape and are combined into curved chains, which, in turn, form flat agglomerates of approximately 350 ± 50 nm in diameter. The resulting Co_3O_4 nanopowder was then employed as a functional ink component for the microplotter printing of the corresponding film on the chip surface. An examination of the final planar structure surface by XRD and Raman spectroscopy confirmed the preservation of the crystal lattice of cobalt(II,III) oxide and the absence of any impurities. At the same time, some decrease in the average CSR size (down to 29 ± 3 nm) was found in contrast to the oxide powder used, which may be associated with the partial dissolution of solid-phase particles in α -terpineol during the functional ink preparation. A similar trend was found when analyzing the film microstructure by scanning electron microscopy: there is a decrease in the average size of the primary particles down to 35 ± 5 nm. This effect resulted in an additional increase in the dispersity of the Co_3O_4 film. In general, the oxide film is characterized by a sufficiently high porosity, which is an important parameter for the receptor components of resistive gas sensors, and the pore size is in a wide range, varying from 10 to 500 nm. In addition, the preservation of the microstructural features and the nature of the hierarchical organization of the synthesized nanoscale cobalt(II,III) oxide after the microplotter printing of the corresponding film was demonstrated. Using AFM, its thickness (~ 5 μm) and mean square surface roughness (46 nm) were determined. The results of KPFM testify to a rather high electric conductivity of the material and allowed us to estimate the work function value of its surface (4.62 eV), which, due to measurements carried out in the ambient atmosphere, is lower than that currently found in the literature. SCM data demonstrate the intergranular character of conductivity. The results of chemosensor measurements showed that the printed Co_3O_4 film at 250°C was characterized by a combination of selectivity and a sufficiently high sensor response ($S = 131\%$ for 100 ppm) to hydrogen sulfide. The material behavior upon H_2S detection in the concentration range of 4–200 ppm was studied, showing an increase in the response value from 38 to 137% when the analyte concentration was increased from 4 to 200 ppm. The response times (t_{90}) correlated well with the above relationship, decreasing from 190 to 9 s. The high reproducibility of the chemoresistive response was also confirmed when detecting hydrogen sulfide. Thus, it was shown that the proposed approach allows not only the synthesis of hierarchically organized cobalt(II,III) oxide nanopowder in an automated mode but also the printing of an oxide film similar in microstructural characteristics, demonstrating a high efficiency as a promising receptor component of a resistive gas sensor to H_2S .

Author Contributions: Conceptualization, N.P.S. and T.L.S.; investigation, T.L.S., N.P.S., P.Y.G., A.S.M., I.S.V., I.A.V. and E.P.S.; writing—original draft preparation, T.L.S., P.Y.G., A.S.M., I.S.V., E.P.S. and N.P.S.; writing—review and editing, T.L.S., I.A.V., E.P.S., N.P.S. and N.T.K.; visualization, T.L.S., N.P.S., P.Y.G., I.S.V. and A.S.M.; supervision, I.A.V., N.P.S., E.P.S. and N.T.K. All authors have read and agreed to the published version of the manuscript.

Funding: This work was supported by the Council on grants of the President of the Russian Federation for state support of young Russian scientists MK-1749.2022.1.3. XRD and SEM studies were carried out using shared experimental facilities supported by the Ministry of Science and Higher Education of the Russian Federation as part of the IGIC RAS state assignment.

Institutional Review Board Statement: Not applicable.

Informed Consent Statement: Not applicable.

Data Availability Statement: Not applicable.

Conflicts of Interest: The authors declare no conflict of interest.

References

1. Raval, D.; Gupta, S.K.; Gajjar, P.N. Detection of H₂S, HF and H₂ Pollutant Gases on the Surface of Penta-PdAs₂ Monolayer Using DFT Approach. *Sci. Rep.* **2023**, *13*, 699. [[CrossRef](#)] [[PubMed](#)]
2. Zhang, M.; Gao, G.; Jiang, Y.; Wang, X.; Long, F.; Cai, T. A Sensor Based on High-Sensitivity Multi-Pass Resonant Photoacoustic Spectroscopy for Detection of Hydrogen Sulfide. *Opt. Laser Technol.* **2023**, *159*, 108884. [[CrossRef](#)]
3. Mokrushin, A.S.; Simonenko, T.L.; Simonenko, N.P.; Gorobtsov, P.Y.; Bocharova, V.A.; Kozodaev, M.G.; Markeev, A.M.; Lizunova, A.A.; Volkov, I.A.; Simonenko, E.P.; et al. Microextrusion Printing of Gas-Sensitive Planar Anisotropic NiO Nanostructures and Their Surface Modification in an H₂S Atmosphere. *Appl. Surf. Sci.* **2022**, *578*, 151984. [[CrossRef](#)]
4. Liu, Y.; Zhou, X.; Shi, H. Sulfur Cycle by In Situ Analysis in the Sediment Biofilm of a Sewer System. *J. Environ. Eng.* **2016**, *142*, C4015011. [[CrossRef](#)]
5. Yin, X.; Gao, M.; Miao, R.; Zhang, L.; Zhang, X.; Liu, L.; Shao, X.; Tittel, F.K. Near-Infrared Laser Photoacoustic Gas Sensor for Simultaneous Detection of CO and H₂S. *Opt. Express* **2021**, *29*, 34258. [[CrossRef](#)]
6. Guo, Y.; Qiu, X.; Li, N.; Feng, S.; Cheng, T.; Liu, Q.; He, Q.; Kan, R.; Yang, H.; Li, C. A Portable Laser-Based Sensor for Detecting H₂S in Domestic Natural Gas. *Infrared Phys. Technol.* **2020**, *105*, 103153. [[CrossRef](#)]
7. Pan, Y.; Zhao, J.; Lu, P.; Sima, C.; Liu, D. Recent Advances in Light-Induced Thermoelastic Spectroscopy for Gas Sensing: A Review. *Remote Sens.* **2022**, *15*, 69. [[CrossRef](#)]
8. John, R.A.B.; Ruban Kumar, A. A Review on Resistive-Based Gas Sensors for the Detection of Volatile Organic Compounds Using Metal-Oxide Nanostructures. *Inorg. Chem. Commun.* **2021**, *133*, 108893. [[CrossRef](#)]
9. Jeong, S.Y.; Kim, J.S.; Lee, J.H. Rational Design of Semiconductor-Based Chemiresistors and Their Libraries for Next-Generation Artificial Olfaction. *Adv. Mater.* **2020**, *32*, 2002075. [[CrossRef](#)] [[PubMed](#)]
10. Galstyan, V.; Moumen, A.; Kumarage, G.W.C.; Comini, E. Progress towards Chemical Gas Sensors: Nanowires and 2D Semiconductors. *Sens. Actuators B Chem.* **2022**, *357*, 131466. [[CrossRef](#)]
11. Chen, F.; Zhang, Y.; Wang, D.; Wang, T.; Zhang, J.; Zhang, D. High Performance Ammonia Gas Sensor Based on Electrospun Co₃O₄ Nanofibers Decorated with Hydrothermally Synthesized MoTe₂ Nanoparticles. *J. Alloy. Compd.* **2022**, *923*, 166355. [[CrossRef](#)]
12. Mandal, S.; Rakibuddin, M.; Ananthakrishnan, R. Strategic Synthesis of SiO₂-Modified Porous Co₃O₄ Nano-Octahedra Through the Nanocoordination Polymer Route for Enhanced and Selective Sensing of H₂ Gas over NO_x. *ACS Omega* **2018**, *3*, 648–661. [[CrossRef](#)] [[PubMed](#)]
13. Vetter, S.; Haffer, S.; Wagner, T.; Tiemann, M. Nanostructured Co₃O₄ as a CO Gas Sensor: Temperature-Dependent Behavior. *Sens. Actuators B Chem.* **2015**, *206*, 133–138. [[CrossRef](#)]
14. Cheng, L.; He, Y.; Gong, M.; He, X.; Ning, Z.; Yu, H.; Jiao, Z. MOF-Derived Synthesis of Co₃O₄ Nanospheres with Rich Oxygen Vacancies for Long-Term Stable and Highly Selective n-Butanol Sensing Performance. *J. Alloy. Compd.* **2021**, *857*, 158205. [[CrossRef](#)]
15. Fan, X.; Xu, Y.; Ma, C.; He, W. In-Situ Growth of Co₃O₄ Nanoparticles Based on Electrospray for an Acetone Gas Sensor. *J. Alloy. Compd.* **2021**, *854*, 157234. [[CrossRef](#)]
16. Liu, H.; Jin, S.; Zhang, K.; Jiang, Y.; Feng, Y.; Li, D.; Tang, P. Tuning the Sensing Selectivity of Mesoporous Hierarchical Ti-Doped Co₃O₄ to Toluene and Xylene via Controlling the Oxygen Defects. *Appl. Surf. Sci.* **2023**, *614*, 156079. [[CrossRef](#)]
17. Yu, H.X.; Guo, C.Y.; Zhang, X.F.; Xu, Y.M.; Cheng, X.L.; Gao, S.; Huo, L.H. Recent Development of Hierarchical Metal Oxides Based Gas Sensors: From Gas Sensing Performance to Applications. *Adv. Sustain. Syst.* **2022**, *6*, 1–21. [[CrossRef](#)]
18. Mirzaei, A.; Ansari, H.R.; Shahbaz, M.; Kim, J.-Y.; Kim, H.W.; Kim, S.S. Metal Oxide Semiconductor Nanostructure Gas Sensors with Different Morphologies. *Chemosensors* **2022**, *10*, 289. [[CrossRef](#)]
19. Lei, Q.; Li, H.; Zhang, H.; Wang, J.; Fan, W.; Cai, L. Three-Dimensional Hierarchical CuO Gas Sensor Modified by Au Nanoparticles. *J. Semicond.* **2019**, *40*, 22101. [[CrossRef](#)]

20. Shin, H.; Ahn, J.; Kim, D.H.; Ko, J.; Choi, S.J.; Penner, R.M.; Kim, I.D. Rational Design Approaches of Two-Dimensional Metal Oxides for Chemiresistive Gas Sensors: A Comprehensive Review. *MRS Bull.* **2021**, *46*, 1080–1094. [[CrossRef](#)]
21. Gupta, V.K.; Alharbie, N.S.; Agarwal, S.; Grachev, V.A. New Emerging One Dimensional Nanostructure Materials for Gas Sensing Application: A Mini Review. *Curr. Anal. Chem.* **2019**, *15*, 131–135. [[CrossRef](#)]
22. Yadav, A.; Singh, P.; Gupta, G. Dimension Dependency of Tungsten Oxide for Efficient Gas Sensing. *Environ. Sci. Nano* **2022**, *9*, 40–60. [[CrossRef](#)]
23. Tomić, M.; Šetka, M.; Vojkúvka, L.; Vallejos, S. Vocs Sensing by Metal Oxides, Conductive Polymers, and Carbon-Based Materials. *Nanomaterials* **2021**, *11*, 552. [[CrossRef](#)] [[PubMed](#)]
24. Jiang, Q.; Guo, X.; Wang, C.; Jia, L.; Zhao, Z.; Yang, R.; Wang, P.; Deng, Q. Polyvinylpyrrolidone-Mediated Co₃O₄ Microspheres Assembled in Size-Tunable Submicron Spheres with Porous Core-Shell Structure for High-Performance Gases Sensing. *J. Alloy. Compd.* **2023**, *935*, 167976. [[CrossRef](#)]
25. Simonenko, T.L.; Bocharova, V.A.; Simonenko, N.P.; Gorobtsov, F.Y.; Simonenko, E.P.; Muradova, A.G.; Sevastyanov, V.G.; Kuznetsov, N.T. Formation of One-Dimensional Hierarchical MoO₃ Nanostructures under Hydrothermal Conditions. *Russ. J. Inorg. Chem.* **2020**, *65*, 459–465. [[CrossRef](#)]
26. Zhang, R.; Gao, S.; Zhou, T.; Tu, J.; Zhang, T. Facile Preparation of Hierarchical Structure Based on P-Type Co₃O₄ as Toluene Detecting Sensor. *Appl. Surf. Sci.* **2020**, *503*, 144167. [[CrossRef](#)]
27. Li, K.; Chang, X.; Qiao, X.; Yu, S.; Li, X.; Xia, F.; Xue, Q. Bimetallic Metal–Organic Frameworks Derived Hierarchical Flower-like Zn-Doped Co₃O₄ for Enhanced Acetone Sensing Properties. *Appl. Surf. Sci.* **2021**, *565*, 150520. [[CrossRef](#)]
28. Hao, F.; Zhang, Z.; Yin, L. Co₃O₄/Carbon Aerogel Hybrids as Anode Materials for Lithium-Ion Batteries with Enhanced Electrochemical Properties. *ACS Appl. Mater. Interfaces* **2013**, *5*, 8337–8344. [[CrossRef](#)]
29. Wang, X.; Sumboja, A.; Khoo, E.; Yan, C.; Lee, P.S. Cryogel Synthesis of Hierarchical Interconnected Macro-/Mesoporous Co₃O₄ with Superb Electrochemical Energy Storage. *J. Phys. Chem. C* **2012**, *116*, 4930–4935. [[CrossRef](#)]
30. Kim, G.; Kim, B.-H. One-Dimensional Hierarchical Porous Carbon Nanofibers with Cobalt Oxide in a Hollow Channel for Electrochemical Applications. *J. Alloy. Compd.* **2022**, *910*, 164886. [[CrossRef](#)]
31. Li, S.; Zhang, J.; Chao, H.; Tan, X.; Wu, X.; He, S.; Liu, H.; Wu, M. High Energy Density Lithium-Ion Capacitor Enabled by Nitrogen-Doped Amorphous Carbon Linked Hierarchically Porous Co₃O₄ Nanofibers Anode and Porous Carbon Polyhedron Cathode. *J. Alloy. Compd.* **2022**, *918*, 165726. [[CrossRef](#)]
32. Yin, X.; Liu, H.; Cheng, C.; Li, K.; Lu, J. MnO₂ Nanosheets Decorated MOF-Derived Co₃O₄ Triangle Nanosheet Arrays for High-Performance Supercapacitors. *Mater. Technol.* **2022**, *37*, 2188–2193. [[CrossRef](#)]
33. Sun, Y.; Wang, C.; Qin, S.; Pan, F.; Li, Y.; Wang, Z.; Qin, C. Co₃O₄ Nanopetals Grown on the Porous CuO Network for the Photocatalytic Degradation. *Nanomaterials* **2022**, *12*, 2850. [[CrossRef](#)] [[PubMed](#)]
34. Li, M.; Wang, Y.; Yang, H.; Chu, P.K. Hierarchical CoMoO₄@Co₃O₄ Nanocomposites on an Ordered Macro-Porous Electrode Plate as a Multi-Dimensional Electrode in High-Performance Supercapacitors. *J. Mater. Chem. A* **2017**, *5*, 17312–17324. [[CrossRef](#)]
35. Yi, H.; Zhang, X.; Zheng, R.; Song, S.; An, Q.; Yang, H. Rich Se Nanoparticles Modified Cobalt Carbonate Hydroxide as an Efficient Electrocatalyst for Boosted Hydrogen Evolution in Alkaline Conditions. *Appl. Surf. Sci.* **2021**, *565*, 150505. [[CrossRef](#)]
36. Wijitwongwan, R.; Intasa-Ard, S.; Ogawa, M. Preparation of Layered Double Hydroxides toward Precisely Designed Hierarchical Organization. *ChemEngineering* **2019**, *3*, 68. [[CrossRef](#)]
37. Wei, C.; Yan, X.; Zhou, Y.; Xu, W.; Gan, Y.; Zhang, Y.; Zhang, N. Morphological Control of Layered Double Hydroxides Prepared by Co-Precipitation Method. *Crystals* **2022**, *12*, 1713. [[CrossRef](#)]
38. Jiang, W.; Pacella, M.S.; Athanasiadou, D.; Nelea, V.; Vali, H.; Hazen, R.M.; Gray, J.J.; McKee, M.D. Chiral Acidic Amino Acids Induce Chiral Hierarchical Structure in Calcium Carbonate. *Nat. Commun.* **2017**, *8*, 15066. [[CrossRef](#)]
39. Yang, H.; Wang, Y.; Liang, T.; Deng, Y.; Qi, X.; Jiang, H.; Wu, Y.; Gao, H. Hierarchical Porous Calcium Carbonate Microspheres as Drug Delivery Vector. *Prog. Nat. Sci. Mater. Int.* **2017**, *27*, 674–677. [[CrossRef](#)]
40. Huang, Y.; Huang, Y.; Li, K.; Chen, W.; Wu, X.; Wu, W.; Huang, L.; Zhao, Q. Synthesis and Electrochemical Properties of Ni_xCo_{3-x}O₄ with Porous Hierarchical Structures for Na-Ion Batteries. *J. Electron. Mater.* **2020**, *49*, 5508–5522. [[CrossRef](#)]
41. Liu, H.; Zhu, G.; Zhang, L.; Qu, Q.; Shen, M.; Zheng, H. Controllable Synthesis of Spinel Lithium Nickel Manganese Oxide Cathode Material with Enhanced Electrochemical Performances through a Modified Oxalate Co-Precipitation Method. *J. Power Sources* **2015**, *274*, 1180–1187. [[CrossRef](#)]
42. Simonenko, T.L.; Simonenko, N.P.; Gorobtsov, P.Y.; Vlasov, I.S.; Solovey, V.R.; Shelaev, A.V.; Simonenko, E.P.; Glumov, O.V.; Melnikova, N.A.; Kozodaev, M.G.; et al. Microplotter Printing of Planar Solid Electrolytes in the CeO₂–Y₂O₃ System. *J. Colloid Interface Sci.* **2021**, *588*, 209–220. [[CrossRef](#)] [[PubMed](#)]
43. Pang, Y.; Cao, Y.; Chu, Y.; Liu, M.; Snyder, K.; MacKenzie, D.; Cao, C. Additive Manufacturing of Batteries. *Adv. Funct. Mater.* **2020**, *30*, 1906244. [[CrossRef](#)]
44. Zhang, H.; Moon, S.K.; Ngo, T.H. 3D Printed Electronics of Non-Contact Ink Writing Techniques: Status and Promise. *Int. J. Precis. Eng. Manuf. Technol.* **2020**, *7*, 511–524. [[CrossRef](#)]
45. Rieu, M.; Camara, M.; Tournier, G.; Viricelle, J.-P.; Pijolat, C.; de Rooij, N.F.; Briand, D. Fully Inkjet Printed SnO₂ Gas Sensor on Plastic Substrate. *Sens. Actuators B Chem.* **2016**, *236*, 1091–1097. [[CrossRef](#)]

46. Homenick, C.M.; James, R.; Lopinski, G.P.; Dunford, J.; Sun, J.; Park, H.; Jung, Y.; Cho, G.; Malenfant, P.R.L. Fully Printed and Encapsulated SWCNT-Based Thin Film Transistors via a Combination of R2R Gravure and Inkjet Printing. *ACS Appl. Mater. Interfaces* **2016**, *8*, 27900–27910. [[CrossRef](#)]
47. Simonenko, E.P.; Mokrushin, A.S.; Simonenko, N.P.; Voronov, V.A.; Kim, V.P.; Tkachev, S.V.; Gubin, S.P.; Sevastyanov, V.G.; Kuznetsov, N.T. Ink-Jet Printing of a TiO₂–10%ZrO₂ Thin Film for Oxygen Detection Using a Solution of Metal Alkoxoacetylacetonates. *Thin Solid Film*. **2019**, *670*, 46–53. [[CrossRef](#)]
48. Kiaee, M.M.; Maeder, T.; Brugger, J. Inkjet-Printed Composites for Room-Temperature VOC Sensing: From Ink Formulation to Sensor Characterization. *Adv. Mater. Technol.* **2021**, *6*, 1–11. [[CrossRef](#)]
49. Zhu, Y.; Yu, L.; Wu, D.; Lv, W.; Wang, L. A High-Sensitivity Graphene Ammonia Sensor via Aerosol Jet Printing. *Sens. Actuators A Phys.* **2021**, *318*, 112434. [[CrossRef](#)]
50. Cabañas, M.V.; Delabouglise, G.; Labeau, M.; Vallet-Regí, M. Application of a Modified Ultrasonic Aerosol Device to the Synthesis of SnO₂ and Pt/SnO₂ for Gas Sensors. *J. Solid State Chem.* **1999**, *144*, 86–90. [[CrossRef](#)]
51. Arsenov, P.V.; Vlasov, I.S.; Efimov, A.A.; Minkov, K.N.; Ivanov, V. V Aerosol Jet Printing of Platinum Microheaters for the Application in Gas Sensors. *IOP Conf. Ser. Mater. Sci. Eng.* **2019**, *473*, 012042. [[CrossRef](#)]
52. Sahm, T.; Rong, W.; Bärtsan, N.; Mädler, L.; Weimar, U. Sensing of CH₄, CO and Ethanol with in Situ Nanoparticle Aerosol-Fabricated Multilayer Sensors. *Sens. Actuators B Chem.* **2007**, *127*, 63–68. [[CrossRef](#)]
53. Zhang, H.; Moon, S.K.; Ngo, T.H. Hybrid Machine Learning Method to Determine the Optimal Operating Process Window in Aerosol Jet 3D Printing. *ACS Appl. Mater. Interfaces* **2019**, *11*, 17994–18003. [[CrossRef](#)] [[PubMed](#)]
54. Gupta, A.A.; Arunachalam, S.; Cloutier, S.G.; Izquierdo, R. Fully Aerosol-Jet Printed, High-Performance Nanoporous ZnO Ultraviolet Photodetectors. *ACS Photonics* **2018**, *5*, 3923–3929. [[CrossRef](#)]
55. Simonenko, T.L.; Simonenko, N.P.; Simonenko, E.P.; Vlasov, I.S.; Volkov, I.A.; Kuznetsov, N.T. Microplotter Printing of Hierarchically Organized Planar NiCo₂O₄ Nanostructures. *Russ. J. Inorg. Chem.* **2022**, *67*, 1848–1854. [[CrossRef](#)]
56. Fedorov, F.S.; Simonenko, N.P.; Trouillet, V.; Volkov, I.A.; Plugin, I.A.; Rupasov, D.P.; Mokrushin, A.S.; Nagornov, I.A.; Simonenko, T.L.; Vlasov, I.S.; et al. Microplotter-Printed On-Chip Combinatorial Library of Ink-Derived Multiple Metal Oxides as an “Electronic Olfaction” Unit. *ACS Appl. Mater. Interfaces* **2020**, *12*, 56135–56150. [[CrossRef](#)]
57. Sobolewski, P.; Goszczynska, A.; Aleksandrak, M.; Urbas, K.; Derkowska, J.; Bartoszewska, A.; Podolski, J.; Mijowska, E.; Fray, M. El A Biofunctionalizable Ink Platform Composed of Catechol-Modified Chitosan and Reduced Graphene Oxide/Platinum Nanocomposite. *Beilstein J. Nanotechnol.* **2017**, *8*, 1508–1514. [[CrossRef](#)]
58. Simonenko, T.L.; Simonenko, N.P.; Gorobtsov, P.Y.; Simonenko, E.P.; Kuznetsov, N.T. Microextrusion Printing of Multilayer Hierarchically Organized Planar Nanostructures Based on NiO, (CeO₂)_{0.8}(Sm₂O₃)_{0.2} and La_{0.6}Sr_{0.4}Co_{0.2}Fe_{0.8}O_{3–δ}. *Micromachines* **2022**, *14*, 3. [[CrossRef](#)]
59. Simonenko, T.L.; Simonenko, N.P.; Gorobtsov, P.Y.; Grafov, O.Y.; Simonenko, E.P.; Kuznetsov, N.T. Synthesis of ((CeO₂)_{0.8}(Sm₂O₃)_{0.2})@NiO Core-Shell Type Nanostructures and Microextrusion Printing of a Composite Anode Based on Them. *Materials* **2022**, *15*, 8918. [[CrossRef](#)]
60. Gorobtsov, P.Y.; Mokrushin, A.S.; Simonenko, T.L.; Simonenko, N.P.; Simonenko, E.P.; Kuznetsov, N.T. Microextrusion Printing of Hierarchically Structured Thick V₂O₅ Film with Independent from Humidity Sensing Response to Benzene. *Materials* **2022**, *15*, 7837. [[CrossRef](#)]
61. Fisenko, N.A.; Solomatov, I.A.; Simonenko, N.P.; Mokrushin, A.S.; Gorobtsov, P.Y.; Simonenko, T.L.; Volkov, I.A.; Simonenko, E.P.; Kuznetsov, N.T. Atmospheric Pressure Solvothermal Synthesis of Nanoscale SnO₂ and Its Application in Microextrusion Printing of a Thick-Film Chemosensor Material for Effective Ethanol Detection. *Sensors* **2022**, *22*, 9800. [[CrossRef](#)] [[PubMed](#)]
62. Simonenko, N.P.; Kadyrov, N.S.; Simonenko, T.L.; Simonenko, E.P.; Sevastyanov, V.G.; Kuznetsov, N.T. Preparation of ZnS Nanopowders and Their Use in the Additive Production of Thick-Film Structures. *Russ. J. Inorg. Chem.* **2021**, *66*, 1283–1288. [[CrossRef](#)]
63. Seo, H.; Nishi, T.; Kishimoto, M.; Ding, C.; Iwai, H.; Saito, M.; Yoshida, H. Study of Microextrusion Printing for Enlarging Electrode–Electrolyte Interfacial Area in Anode-Supported SOFCs. *ECS Trans.* **2019**, *91*, 1923–1931. [[CrossRef](#)]
64. Mokrushin, A.S.; Fisenko, N.A.; Gorobtsov, P.Y.; Simonenko, T.L.; Glumov, O.V.; Melnikova, N.A.; Simonenko, N.P.; Bukunov, K.A.; Simonenko, E.P.; Sevastyanov, V.G.; et al. Pen Plotter Printing of ITO Thin Film as a Highly CO Sensitive Component of a Resistive Gas Sensor. *Talanta* **2021**, *221*, 121455. [[CrossRef](#)] [[PubMed](#)]
65. Liu, S.; Cao, R.; Wu, J.; Guan, L.; Li, M.; Liu, J.; Tian, J. Directly Writing Barrier-Free Patterned Biosensors and Bioassays on Paper for Low-Cost Diagnostics. *Sens. Actuators B Chem.* **2019**, *285*, 529–535. [[CrossRef](#)]
66. Liang, R.; Yonezawa, S.; Kim, J.-H.; Inoue, T. Low-Temperature Synthesis of LiCoO₂ with Eutectic of Lithium Precursors via the Solid-State Reaction Method. *J. Asian Ceram. Soc.* **2018**, *6*, 332–341. [[CrossRef](#)]
67. Vidhya, M.S.; Ravi, G.; Yuvakkumar, R.; Velauthapillai, D.; Thambidurai, M.; Dang, C.; Saravanakumar, B. Nickel–Cobalt Hydroxide: A Positive Electrode for Supercapacitor Applications. *RSC Adv.* **2020**, *10*, 19410–19418. [[CrossRef](#)]
68. Rahimi, S.A.; Norouzi, P.; Ganjali, M.R. One-Step Cathodic Electrodeposition of a Cobalt Hydroxide–Graphene Nanocomposite and Its Use as a High Performance Supercapacitor Electrode Material. *RSC Adv.* **2018**, *8*, 26818–26827. [[CrossRef](#)]
69. Shi, X.; Quan, S.; Yang, L.; Liu, C.; Shi, F. Anchoring Co₃O₄ on BiFeO₃: Achieving High Photocatalytic Reduction in Cr(VI) and Low Cobalt Leaching. *J. Mater. Sci.* **2019**, *54*, 12424–12436. [[CrossRef](#)]
70. Abdallah, A.M.; Awad, R. Study of the Structural and Physical Properties of Co₃O₄ Nanoparticles Synthesized by Co-Precipitation Method. *J. Supercond. Nov. Magn.* **2020**, *33*, 1395–1404. [[CrossRef](#)]

71. Wang, L.; Fu, J.; Zhang, Y.; Liu, X.; Yin, Y.; Dong, L.; Chen, S. Mesoporous β -Co(OH)₂ Nanowafers and Nanohexagonals Obtained Synchronously in One Solution and Their Electrochemical Hydrogen Storage Properties. *Prog. Nat. Sci. Mater. Int.* **2016**, *26*, 555–561. [[CrossRef](#)]
72. Sun, J.; Wang, H.; Li, Y.; Zhao, M. Porous Co₃O₄ Column as a High-Performance Lithium Anode Material. *J. Porous Mater.* **2021**, *28*, 889–894. [[CrossRef](#)]
73. Liu, X.; Qu, B.; Zhu, F.; Gong, L.; Su, L.; Zhu, L. Sonochemical Synthesis of β -Co(OH)₂ Hexagonal Nanoplates and Their Electrochemical Capacitive Behaviors. *J. Alloy. Compd.* **2013**, *560*, 15–19. [[CrossRef](#)]
74. Wang, Y.; Wei, X.; Hu, X.; Zhou, W.; Zhao, Y. Effect of Formic Acid Treatment on the Structure and Catalytic Activity of Co₃O₄ for N₂O Decomposition. *Catal. Lett.* **2019**, *149*, 1026–1036. [[CrossRef](#)]
75. Rashad, M.; Rüsing, M.; Berth, G.; Lischka, K.; Pawlis, A. CuO and Co₃O₄ Nanoparticles: Synthesis, Characterizations, and Raman Spectroscopy. *J. Nanomater.* **2013**, *2013*, 1–6. [[CrossRef](#)]
76. Liu, J.; Ke, J.; Li, Y.; Liu, B.; Wang, L.; Xiao, H.; Wang, S. Co₃O₄ Quantum Dots/TiO₂ Nanobelt Hybrids for Highly Efficient Photocatalytic Overall Water Splitting. *Appl. Catal. B Environ.* **2018**, *236*, 396–403. [[CrossRef](#)]
77. Liu, M.; Liu, J.; Li, Z.; Wang, F. Atomic-Level Co₃O₄ Layer Stabilized by Metallic Cobalt Nanoparticles: A Highly Active and Stable Electrocatalyst for Oxygen Reduction. *ACS Appl. Mater. Interfaces* **2018**, *10*, 7052–7060. [[CrossRef](#)] [[PubMed](#)]
78. Creazzo, F.; Galimberti, D.R.; Pezzotti, S.; Gaigeot, M.-P. DFT-MD of the (110)-Co₃O₄ Cobalt Oxide Semiconductor in Contact with Liquid Water, Preliminary Chemical and Physical Insights into the Electrochemical Environment. *J. Chem. Phys.* **2019**, *150*, 041721. [[CrossRef](#)]
79. Kim, H.-J.; Lee, J.-H. Highly Sensitive and Selective Gas Sensors Using P-Type Oxide Semiconductors: Overview. *Sens. Actuators B Chem.* **2014**, *192*, 607–627. [[CrossRef](#)]
80. Navale, S.T.; Liu, C.; Gaikar, P.S.; Patil, V.B.; Sagar, R.U.R.; Du, B.; Mane, R.S.; Stadler, F.J. Solution-Processed Rapid Synthesis Strategy of Co₃O₄ for the Sensitive and Selective Detection of H₂S. *Sens. Actuators B Chem.* **2017**, *245*, 524–532. [[CrossRef](#)]
81. Balouria, V.; Samanta, S.; Singh, A.; Debnath, A.K.; Mahajan, A.; Bedi, R.K.; Aswal, D.K.; Gupta, S.K. Chemiresistive Gas Sensing Properties of Nanocrystalline Co₃O₄ Thin Films. *Sens. Actuators B Chem.* **2013**, *176*, 38–45. [[CrossRef](#)]
82. Srivastava, R.K.; Lal, P.; Dwivedi, R.; Srivastava, S.K. Sensing Mechanism in Tin Oxide-Based Thick-Film Gas Sensors. *Sens. Actuators B Chem.* **1994**, *21*, 213–218. [[CrossRef](#)]
83. Simonenko, T.L.; Simonenko, N.P.; Gorobtsov, P.Y.; Mokrushin, A.S.; Solovey, V.R.; Pozharnitskaya, V.M.; Simonenko, E.P.; Glumov, O.V.; Melnikova, N.A.; Lizunova, A.A.; et al. Pen Plotter Printing of Co₃O₄ Thin Films: Features of the Microstructure, Optical, Electrophysical and Gas-Sensing Properties. *J. Alloy. Compd.* **2020**, *832*, 154957. [[CrossRef](#)]
84. Cui, G.; Zhang, P.; Chen, L.; Wang, X.; Li, J.; Shi, C.; Wang, D. Highly Sensitive H₂S Sensors Based on Cu₂O/Co₃O₄ Nano/Microstructure Heteroarrays at and below Room Temperature. *Sci. Rep.* **2017**, *7*, 43887. [[CrossRef](#)]
85. Shi, T.; Hou, H.; Hussain, S.; Ge, C.; Alsaiani, M.A.; Alkorbi, A.S.; Liu, G.; Alsaiani, R.; Qiao, G. Efficient Detection of Hazardous H₂S Gas Using Multifaceted Co₃O₄/ZnO Hollow Nanostructures. *Chemosphere* **2022**, *287*, 132178. [[CrossRef](#)]
86. Moon, S.; Vuong, N.M.; Lee, D.; Kim, D.; Lee, H.; Kim, D.; Hong, S.-K.; Yoon, S.-G. Co₃O₄-SWCNT Composites for H₂S Gas Sensor Application. *Sens. Actuators B Chem.* **2016**, *222*, 166–172. [[CrossRef](#)]

Disclaimer/Publisher's Note: The statements, opinions and data contained in all publications are solely those of the individual author(s) and contributor(s) and not of MDPI and/or the editor(s). MDPI and/or the editor(s) disclaim responsibility for any injury to people or property resulting from any ideas, methods, instructions or products referred to in the content.